Environmental and Climate Technologies
2025, vol. 29, no. 1, pp. 960–976
https://doi.org/10.2478/rtuect-2025-0064
https://content.sciendo.com

1862
RIGA TECHNICAL UNIVERSITY

Experimental and Mathematical Modelling of Bulk Amorphous Structure Formation in Multi-Component Alloys via Twin-Roll Rapid Solidification

Hanna KOSHLAK[1*], Miroslav RIMÁR[2]

[1]*Kielce University of Technology, Al. Tysiąclecia Państwa Polskiego 7, 25-314 Kielce, Poland*
[2]*Technical University of Košice, Letná 1/9, 040 01, Košice, Slovakia*

Received 02.10.2025; accepted 12.11.2025

***Abstract* – This study investigates the formation processes of amorphous layers via twin-roll rapid solidification, focusing on the critical factors that govern the conversion of the melt into a solid amorphous phase. The core objective was to identify and optimise the critical processing parameters that govern the melt's conversion into a solid amorphous phase. The $Ni_{62.4}Nb_{37.6}$ alloy was selected as the model system, notably possessing a relatively low critical cooling rate in the range of R_c from 10^2 to 10^3 K/s. Through experimental trials, this process successfully yielded a bulk amorphous layer, which was subsequently confirmed by comprehensive metallophysical characterisation. Key variables such as the gap between the rollers, roller speed, and cooling air temperature were systematically investigated. The experimental analysis determined the degree of amorphisation Ψ that could be achieved, with optimal conditions yielding values up to 6. Furthermore, a detailed mathematical model was developed and employed to precisely determine the thermal fields and optimise the essential technological parameters by correlating them with the local cooling kinetics. The resulting amorphous microstructures obtained by this method are high-performance materials, demonstrating a remarkable Vickers hardness of 740 HV, confirming the viability of this technique for developing next-generation structural materials.**

***Keywords* – Amorphous structure; bulk metallic glass; critical cooling rate; mathematical modelling; rapid solidification; twin-roll casting; Vickers hardness.**

1. INTRODUCTION

The amorphous state represents a thermodynamically metastable phase characterized by a disordered, non-crystalline atomic arrangement. This isotropic local structure imparts unique physical, chemical, and mechanical properties to amorphous materials, often surpassing their crystalline counterparts. Notably, the metastable nature of metallic glasses is responsible for their exceptional properties, including high strength, remarkable corrosion resistance, and superior wear resistance [1]–[4], positioning them as highly promising engineering and structural materials for diverse applications [5]–[8].

The key determinant for the formation of an amorphous structure is the critical cooling rate R_c of the liquid melt [9], [10]. Conventional rapid solidification techniques, such as melt spinning or planar flow casting, rely on short-duration heat extraction to achieve the requisite

* Corresponding author.
E-mail address: hkoshlak@tu.kielce.pl

©2025 Author(s). This is an open access article licensed under the Creative Commons Attribution License (http://creativecommons.org/licenses/by/4.0).

high cooling rates, typically in the range of 10^4 to 10^6 K/s for many alloys, with pure metals requiring rates often exceeding 10^6 K/s. The principle involves contacting a molten metal layer with a high-conductivity chill body, leading to the formation of various metastable structural states during subsequent solidification [16], [17].

However, most established cooling methods are designed for synthesizing amorphous materials structures only in thin superficial layers or foils [18], [19]. This is a significant limitation, as the necessary high-velocity heat removal from the melt becomes substantially more complex and less efficient as the thickness of the material increases. The key technological challenge for industrial uptake lies in the reliable synthesis of massive or bulk amorphous structures (BMGs). Achieving size scalability requires maintaining an ultra-high cooling rate deep within the material volume, which often necessitates costly and complex processing or the use of specific, high-purity alloy compositions.

Recent research has focused on developing alloys with an improved glass-forming ability, such as Ti-, Zr-, Cu-, and Ni-based BMGs, which exhibit lower R_c values, sometimes below 250 K/s [20]. For instance, Ni- Nb-based BMGs have shown potential, reaching critical casting thicknesses up to 5 mm when combined with metalloids like Ni-Nb-P system [21]. However, the reliable, scalable production of such components demands rigorous process control and optimisation.

This study addresses the aforementioned technological and scientific gap by investigating the synthesis of amorphous materials structures using the twin-roll rapid solidification (TRRS) technique. TRRS is a promising, near-net-shape process that offers advantages in continuous manufacturing and provides the required near-rapid cooling rates $R_c \approx 10^3$ K/s, while concurrently facilitating solidification and deformation [22].

To establish the necessary process control, our work adopts an innovative, integrated approach combining experimental investigation with a sophisticated dual mathematical modelling system. This research specifically focuses on:

- experimental verification of structure formation in selected glass-forming alloys, including Cu- and Ni-based systems;
- the development of coupled thermal-fluid models (based on heat conduction and Navier-Stokes equations) to quantitatively understand and predict the temperature fields, cooling kinetics, and the resulting structure across the bulk material thickness;
- optimisation of key process parameters to maximize the degree of amorphisation.

2. MATERIALS AND METHODS

2.1. Experimental Setup and Material Selection

This investigation employed the twin-roll rapid solidification technique with the aim of synthesizing bulk amorphous structures. Given that existing literature predominantly focuses on the synthesis of thin amorphous layers [23]–[25], a dedicated experimental laboratory setup (Fig. 1) was developed and utilized to achieve and control the necessary high cooling rates for massive sections.

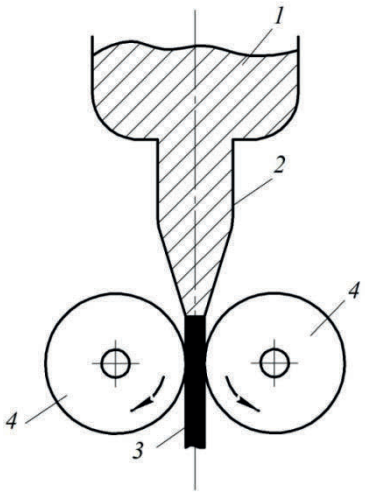

Fig. 1. Schematic diagram of the twin-roll rapid solidification process, illustrating the key components and melt flow dynamics: 1 – liquid metal melt; 2 – feeder nozzle; 3 – cooling metal layer; 4 – chilled copper rollers.

The experimental setup utilized two rotating chilled copper rollers (4) moving at a peripheral speed in the range of 200 to 500 rev/min, between which the liquid metal (1) was poured using a specialized feeder (2). The process was influenced by three key control factors: the gap between the rollers H (defining the melt thickness), the roller rotation speed ω, and the temperature of the humid cooling air T_a.

Four distinct glass-forming alloys were selected for the investigation, prepared from high-purity powder components: $Cu_{45}Ti_{35}Zr_{20}$, $Ni_{62.4}Nb_{37.6}$, $Fe_{80}P_{13}C_7$, $Co_{75}Si_{15}B_{10}$.

2.2. Characterisation Techniques and Experimental Design

To evaluate the resulting structure and quantify the degree of amorphisation Ψ, samples were prepared for analysis across a series of transverse cross-sections. Microstructural analysis involved chemical etching using a solution of CH_3-COOH, HNO_3 and HF. Microscopic observation and documentation were performed using the MMP-4 microscope.

The degree of amorphisation was determined via electron-microscopic investigations conducted in a direct expansion mode. Thermal stability and the solidification process were studied using a Setaram DSC 131 differential scanning calorimeter; thermal data analysis utilized the instrument's dedicated software package. Structure interpretation for some phases was carried out using the Waseda methodology.

The experimental data related to the influence of control factors on the degree of amorphisation was processed using design of experiments methodology. The established ranges for the control factors are summarized in Table 1.

TABLE 1. RANGES OF CONTROL FACTORS

Factor	Units	Defining range	Permissible range
Roller gap, H	mm	2–10	2–10
Humid cooling air temperature, T_a	°C	20–50	20–50
Roller rotation speed, ω	rev/min	200–500	200–500

3. Experimental Results and Discussion

3.1. Analysis of Structure Formation

Metallographic analysis confirmed that the primary structural phases obtained via TRRS were highly dependent on the processing parameters. When the roller gap was maximum H = 10 mm and the air temperature and roller speed were minimal, a low cooling rate resulted. This condition yielded a ferritic microcrystalline structure (MCS) (Fig. 2), with no discernible amorphous phase formation.

Fig. 2. Microcrystalline structure (MCS) observed within the massive, solidified layer, typically obtained under conditions of low cooling rate, maximum roller gap H = 10 mm.

By significantly reducing the humid air temperature and the roller gap, while maintaining or increasing the roller speed, the heat extraction intensity was substantially enhanced. This led to the formation of a partial amorphous structure along the layer boundaries adjacent to the chilled rollers, with a complex ferrite-perlite crystalline structure (including martensite, bainite, and retained austenite) forming in the centre (Fig. 3).

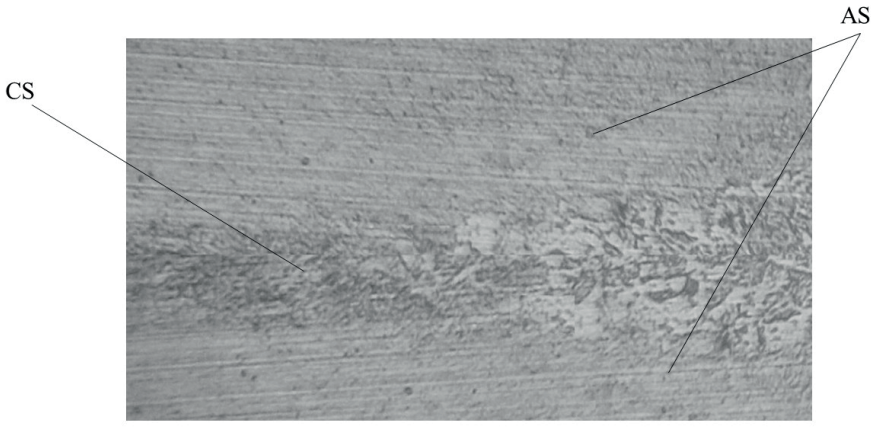

Fig. 3. Amorphous-crystalline composite structure observed in the massive metal layer, obtained under conditions promoting high heat extraction (minimum roller gap and reduced cooling air temperature).

The experimental data related to the influence of the three primary control factors on the resultant degree of amorphisation Ψ were subjected to a design of experiments analysis. This analysis successfully highlighted the synergistic influence of the processing parameters on the overall amorphisation kinetics. The roller gap H, which dictates the final melt thickness, was unequivocally identified as the primary and most critical factor governing Ψ. This factor directly controls the heat diffusion length, confirming that minimizing H is essential for maximizing the average cooling rate across the section and achieving the highest degree of amorphisation.

The combined effect of the humid cooling air temperature T_a and the roller rotation speed ω also significantly impacted Ψ (Fig. 4).

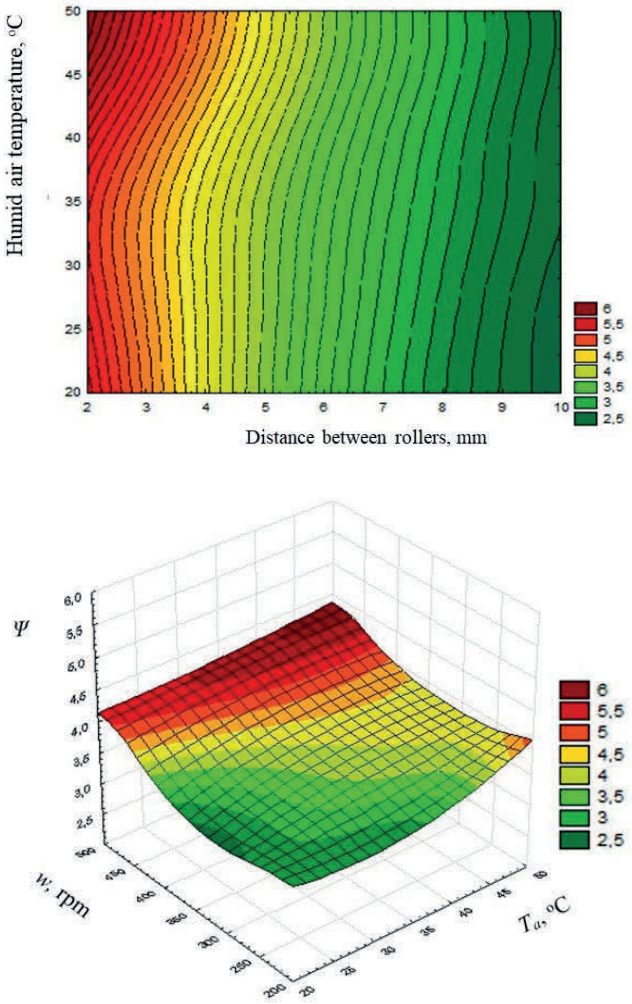

Fig. 4. Graphical dependence of the degree of amorphisation Ψ on the humid cooling air temperature T_a and the roller rotation speed ω, illustrating the combined effect of key technological parameters on the amorphisation kinetics of the massive solidified layer.

The highest surface cooling rates were achieved under conditions of maximum ω and maximum T_a, as these conditions maximize the intensity and duration of contact between the melt surface and the chilled copper rollers.

The results demonstrated that a significant degree of amorphisation, reaching Ψ≈4, could be sustained even with a relatively large roller gap of 5.5 mm. This observation is critical as it strongly supports the viability of bulk amorphous structure formation in the TRRS process, provided the air temperature T_a is maintained at a maximal level 50 °C. This finding fundamentally reinforces the hypothesis that heat extraction efficiency is paramount and must be aggressively maintained, particularly when dealing with increased melt thickness. The observed structural gradient resulting in mixed amorphous-crystalline (AS/CS) structures is fundamentally explained by the temperature differential across the layer's thickness. The centre of the massive layer experiences higher temperatures and a significantly longer cooling duration (estimated at 5 to 10 times greater) compared to the surface zones. This prolonged solidification time allows for the initiation and growth of crystalline phases in the central region, even when the surface successfully vitrifies.

4. Mathematical Modelling of Melt Cooling during Twin-Roll Solidification

The formation of a continuous solidified layer during twin-roll rapid solidification (TRRS) is a complex process integrating multiple phenomena, including heat transfer, mass transfer, and internal fluid dynamics in both the liquid and solid phases. The process irreversibility is inherently linked to the transfer of heat and mass, as well as internal movement within the solid and liquid zones. A quantitative description of this solidification process necessitates the application of non-equilibrium thermodynamics principles to a heterogeneous, non-isolated system comprising multiple components and phases [26]–[28].

The cooling of the melt between the rollers (Fig. 1) can be conceptualized as the flow of a narrow, incompressible liquid layer between two elastic-plastic surfaces (the rollers), moving at a controlled speed. For any arbitrary point within the solidifying layer, there is a continuous change in temperature, pressure, velocity, and distance to the transition boundary between the liquid and solid states.

4.1. Mathematical Formalisation for Amorphous Structure Formation in a Planar Slab

Since the dynamics of the continuously cast layer are intrinsically coupled with the heat exchange problem, the fundamental governing equation is the general heat conduction equation for a moving continuum [29]–[31]. This formulation incorporates distributed heat sources resulting from the phase transition, which are dependent on the latent heat of transition and Fourier's law of heat conduction, $q = -\lambda(T)\,\mathrm{grad}T$:

$$\rho\frac{\partial}{\partial t}\left[\, c(T)T - L\Psi \right] = \mathrm{div}\left[\lambda \mathrm{grad}T\right] + Q_v, \tag{1}$$

where

ρ density, kg/m^3;
c specific heat capacity, J/kg·K;
λ thermal conductivity, W/m·K;
T temperature, K;
L specific latent heat of phase transition (crystallization or melting), J/kg;

Ψ solid phase fraction ($\Psi = 0$ for liquid, $\Psi = 1$ for solid, and $0 < \Psi < 1$ in the mushy zone);

Q_v (x, y, z, t) is a function characterizing the heat released during the cooling of the continuously cast metal layer W/m^3.

To obtain a unique solution to the posed problem, the governing equation must be supplemented with appropriate boundary and initial conditions.

The initial condition specifies the temperature distribution at the beginning of the process ($t = 0$), $T(x,0) = T_{\text{initial}}$, where $T_{\text{initial}} \approx 1442$ K.

The boundary conditions are:

– symmetry boundary (centreline, $x = 0$):

$$\lambda_m \frac{\partial T}{\partial x} = 0, \tag{2}$$

– cooling surface boundary ($x = \frac{H}{2}$)

$$\lambda_{\text{m}} \frac{\partial T}{\partial x} = h\left(T_{\text{m}} - T_{\text{a}}\right), \tag{3}$$

where

T_{m} metal temperature, K;

T_{a} ambient air temperature, K;

h heat transfer coefficient, W/m^2·K.

The crucial Stefan boundary condition must be applied at the moving interface, $\xi(t)$, which separates the solid metal phase from the liquid melt phase. This condition accounts for the latent heat release during the phase transition (solidification):

$$\lambda_1 \left.\frac{\partial T_1}{\partial x}\right|_{x=\xi(t)} - \lambda_2 \left.\frac{\partial T_2}{\partial x}\right|_{x=\xi(t)} = \rho L \frac{d\xi}{dt}, \tag{4}$$

where

$\xi(t)$ represents the equation of the phase boundary curve separating the solid metal from the liquid melt;

T_1, T_2 are the temperatures of the solid phase and the liquid phase, K, respectively;

λ_1, λ_2 are the thermal conductivity coefficients of the solid and liquid phases, respectively, W/m·K.

We proceed to determine the functional form of the phase interface curve, $\xi(t)$. We seek a solution to the heat conduction equation by applying the following self-similar (automodel) form:

$$T\left(t,x\right) = f\left(z\right), \tag{5}$$

where

$$z = \frac{x}{\sqrt{t}}.$$

Substituting (5) into the Stefan boundary condition (2) yields the following ordinary differential equation:

$$-\frac{1}{2}\dot{f}(z)\cdot\ z=\alpha\left(\ddot{f}(z)+\frac{1}{z}\dot{f}(z)\right), \tag{7}$$

where $\alpha=\dfrac{\lambda}{\rho c}$ is the thermal diffusivity coefficient.

From this substitution, we obtain

$$\lambda_1\frac{1}{\sqrt{t}}\dot{f}_1\left(\frac{\xi(t)}{\sqrt{t}}\right)-\lambda_2\frac{1}{\sqrt{t}}\dot{f}_2\left(\frac{\xi(t)}{\sqrt{t}}\right)=\rho L\frac{d\xi}{dt}. \tag{8}$$

Assuming the phase boundary separates as:

$$\frac{\xi(t)}{\sqrt{t}}=\alpha=\text{const},\ \lambda_1\dot{f}_1(\alpha)-\lambda_2\dot{f}_2(\alpha)=\rho L\frac{d\xi}{dt}, \tag{9}$$

which implies the phase boundary equation is:

$$\xi(t)=\alpha\sqrt{t}, \tag{10}$$

where α is a constant characteristic of the solidification kinetics. The coefficient α is determined either empirically or by solving the transcendental Eq. (9) for a known value of *L*, the latent heat of aggregation for the liquid-to-solid phase transition.

Knowing the equation of the moving phase boundary ξ(*t*), which separates the liquid melt from the solid metal phase, the solution to the original problem can be simplified to solving the heat conduction equation with a generalised thermal conductivity coefficient:

$$\frac{\partial T}{\partial t}=\lambda(t,x)\left(\frac{\partial^2 T}{\partial x^2}\right), \tag{11}$$

where the effective thermal conductivity coefficient, λ(*t*,*x*), is defined piecewise:

$$\lambda(t,x)\begin{cases}\lambda_1, & \text{if } 0\le x<R \quad \text{solid phase}\\ \lambda_2, & \text{if } R\le x<R+\xi(t) \text{ liquid/melt phase}\end{cases}=\lambda(t,x)\left(\frac{\partial^2 T}{\partial x^2}\right). \tag{12}$$

The necessary initial conditions for this simplified model are defined as:

$$\begin{cases} T\big|_{t=0}=T_{\text{melt}} & \text{for } 0\le x<R\\ T\big|_{t=0}=T_{\text{roller}} & \text{for } R\le x<R+\xi(t)\end{cases}. \tag{13}$$

The computational model was implemented using the C++ programming language. The resulting calculations allowed for the precise determination of the zones (and their respective widths) corresponding to the amorphous, crystalline, and microcrystalline structures. Furthermore, the model yielded the complete distribution of temperatures and cooling rates for the investigated alloys, which are presented in Fig. 5 and Fig. 6.

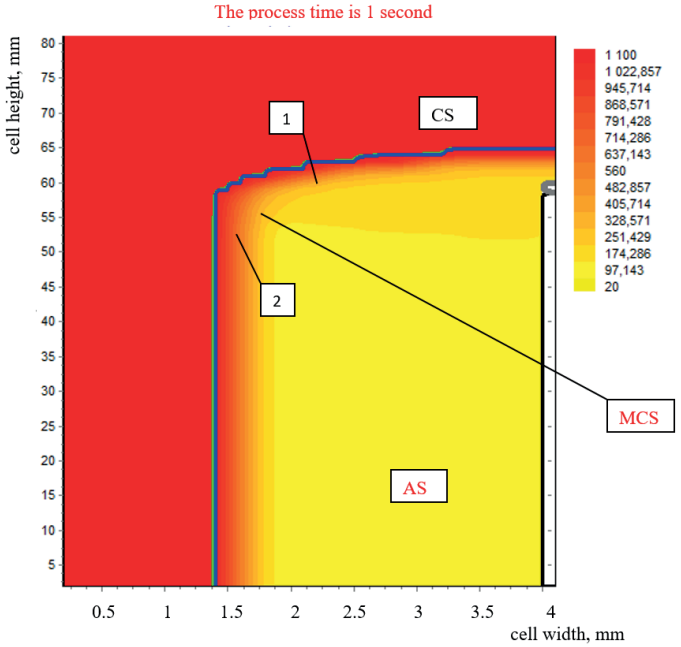

Fig. 5. Temperature field evolution during the $Cu_{45}Ti_{35}Zr_{20}$ melt cooling process, as determined by the mathematical model: 1 – liquidus temperature the line of complete melting, above which only the liquid phase exists; 2 – the line on the phase diagram below which the material is fully solidified (only solid phase exists); AS – amorphous structure zone; CS – crystalline structure zone; MCS – microcrystalline structure zone.

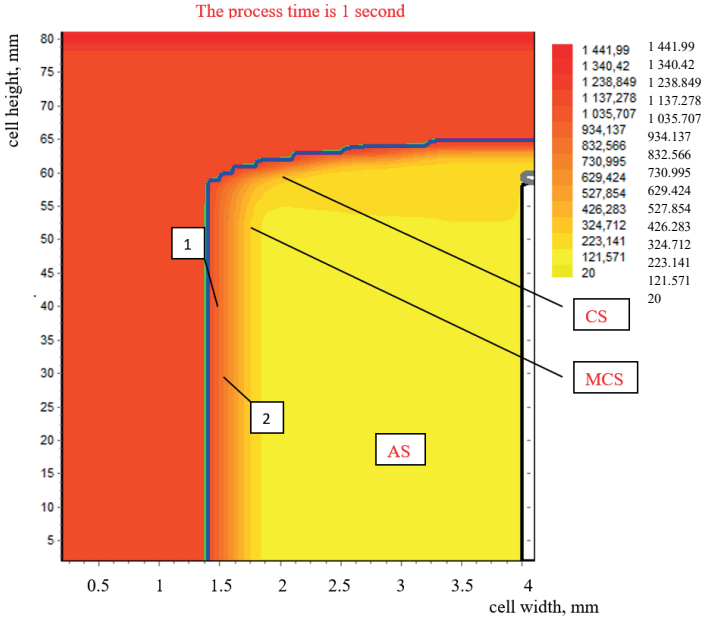

Fig. 6. Temperature field evolution during the $Ni_{62.4}Nb_{37.6}$ melt cooling process, as determined by the mathematical model. Indicators and phase boundaries:1 – liquidus temperature; 2 – solidus temperature; AS – amorphous structure zone; CS – crystalline structure zone; MCS – microcrystalline structure zone.

In the twin-roll rapid solidification (TRRS) technology, experimental evidence has consistently demonstrated that the formation of a fully amorphous structure (AS) is typically confined to the boundaries of the layer, specifically near the interface with the chilled copper rollers. Achieving bulk amorphization necessitates the application of additional auxiliary factors designed to enhance heat exchange processes and substantially increase the intensity of heat extraction. These external factors directly influence the cooling rate of the melt, which is the primary determinant for glass formation.

4.2. Mathematical Formalisation for Amorphous Structure Formation in a Cylindrical Rod

By employing modern methods and tools of mathematical modelling, it is possible to address complex heat transfer tasks, investigate the specific features of the technological process, and reveal the qualitative picture of interaction among various influencing factors. This approach provides the capability to establish quantitative functional dependencies through numerical calculation [32], [33].

The mathematical model developed for the cylindrical geometry is based on solving a coupled system of differential equations for heat conduction and the Navier–Stokes equations governing the flow of a weakly compressible fluid [34], [35]:

– general heat conduction equation (energy conservation)

$$\rho C_{\mathrm{p}} \frac{\partial T}{\partial t} + \nabla\left(-\lambda \nabla T\right) = Q + q_{\mathrm{s}} T\,, \tag{14}$$

where

q_{s} is the absorption coefficient, W/m^3·K;
C_{p} is the specific heat capacity at constant pressure, J/kg·K;
λ the thermal conductivity coefficient, W/m·K;
T temperature, K;
Q heat source, W/m^3;
∇ Nabla operator.

– Navier–Stokes Equation

$$\rho \frac{\partial u}{\partial t} + \rho\left(u\nabla\right)u = \nabla\left[-pI + \mu\left(\nabla u + \left(u\nabla\right)^{T} \right) - \frac{2}{3}\mu\left(\nabla u\right) I \right] + F\,, \tag{15}$$

where

u velocity vector, m/s;
I identity tensor;
μ dynamic viscosity, Pa·s;
F external specific volume force field vector, H/m^3;
p pressure, Pa;
t time, s.

$$\frac{\partial \rho}{\partial t} + \nabla\left(\rho \mathrm{u}\right) = 0\,. \tag{16}$$

Accurate, operational information regarding temperature gradients within the melt is of significant practical importance. This data enables operation with optimally low degrees of superheating, thus ensuring the necessary final structure and high quality of the finished product [36], [37].

It is known that calculating the liquidus temperature T_L does not pose significant difficulties. However, the specified chemical composition of the metal is often achieved only towards the end of the technological process, which severely limits the utility of experimental data for real-time control. Meanwhile, selecting a single universal method for calculating these temperatures presents considerable difficulties in practice, as recommendations from specialists addressing this problem remain quite contradictory [38], [39]. Calculation results confirm that, with a differentiated approach to selecting the formulas used, the calculated temperature values can approximate experimental data quite satisfactorily.

Before discussing amorphous metals, it is necessary to define the physical meaning of the term “melting temperature”. In the scientific and production spheres, this concept is also used as the “solidification temperature”. The physical essence of the process is that this temperature indicates the value at which the substance changes its state of aggregation, transitioning from liquid to solid. At the exact point of temperature transition, the substance can exist in both states. The substance acquires a liquid state when additional heat is supplied, and solidifies when heat is removed. This parameter is considered one of the most important in the system of physical properties of any substance. It is particularly crucial to understand that the solidification temperature is numerically equal to the melting temperature only in the case of ideally pure substances (this is especially important in the context of steels).

A necessary condition for solving the model equations is knowledge of the thermophysical properties of metals and alloys at high temperatures, including specific heat capacity C_p, thermal conductivity λ, and heat of solidification (vitrification). The temperature distribution and flow dynamics within the solidifying ribbon are determined by solving the coupled system of Eqs. (14)–(16).

4.3. Selection of Model Alloys and Geometric Parameters

Model alloys were selected based on their good glass-forming ability, resulting from the inclusion of easily amorphising elements such as Zr, B, P, and Si, which are known amorphisers. Additionally, certain alloys from the Fe and Co groups were chosen, supplemented with metalloid amorphising agents like B, P, Si, and C [40]–[42]. Previous studies have shown that the melt thickness significantly influences the properties and final structure of metals and alloys during amorphous structure formation [43]–[45]. Based on this understanding, four distinct cooling moulds (geometries) with varying dimensions were selected for investigation, as these dimensions directly determined the melt thickness and the potential for achieving an amorphous structure. The thermophysical properties of the investigated alloys are presented in Table 2.

TABLE 2. THERMOPHYSICAL PROPERTIES OF THE INVESTIGATED ALLOYS

Alloy	**Melting temperature, T_m, K**	**Glass transition temperature, T_g, K**	**Alloy density, ρ, kg/m^3**	**Alloy specific heat capacity, C_p, J/kg K**	**Thermal conductivity coefficient, λ, W/m·K**
$Cu_{45}Ti_{35}Zr_{20}$	1336	683	6900	513.9	175
$Ni_{62,4}Nb_{37,6}$	1442	945	7850	609	69
$Fe_{80}P_{13}C_7$	1258	736	6690	720	38.5

The bulk metallic glass alloy from the $Cu_{45}Ti_{35}Zr_{20}$ system is of particular interest. It differs from other bulk amorphous alloys by exhibiting high hardness, strength, and thermal stability. Notably, increasing the Zr content up to 18 % enhances the thermal stability of the alloy, raising the glass transition temperature from 690 K to 815 K, which significantly broadens

the application scope of this alloy group. The formation of an amorphous structure in this specific case is considered a rather complex and ambiguous process. The casting conditions used for solving the thermal problem of the $Cu_{45}Ti_{35}Zr_{20}$ alloy are summarized in Table 3.

TABLE 3. THERMOPHYSICAL PROPERTIES OF THE INVESTIGATED ALLOYS

Parameter name	**Parameter value**	**Unit**
Melt temperature before casting process	1336	K
Temperature of the cooling mould walls	373; 473; 673	K
Casting velocity	1.6	m/s
Melt density, ρ	6900	kg/m^3
Metal specific heat capacity, C_p	513.9	J/kg·K
Dynamic viscosity, μ	0.0434	Pa s
Latent heat of phase transition, L	205	kJ/kg
Thermal conductivity coefficient, λ	175	W/m·K
Measurement interval of the casting process	0–1	s

4.4. Analysis of Simulation Results and Discussion

The modelling results, presented as graphs and temperature distribution fields, are shown in Figs. 7–9. These obtained graphs provide an effective assessment of the heat transfer intensity during the casting process, allowing for the evaluation and prediction of the alloys' structural amorphisation capability.

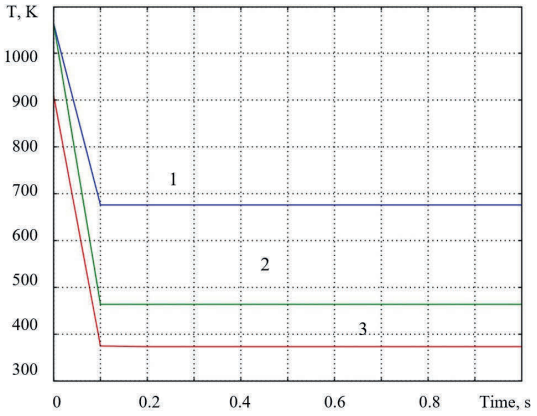

Fig. 7. Temperature distribution in the $Cu_{45}Ti_{35}Zr_{20}$ alloy with a roller surface temperature of 373 K: 1 – casting centre, 2 – near the cooled mould wall, 3 – near the boundary with the cooling medium.

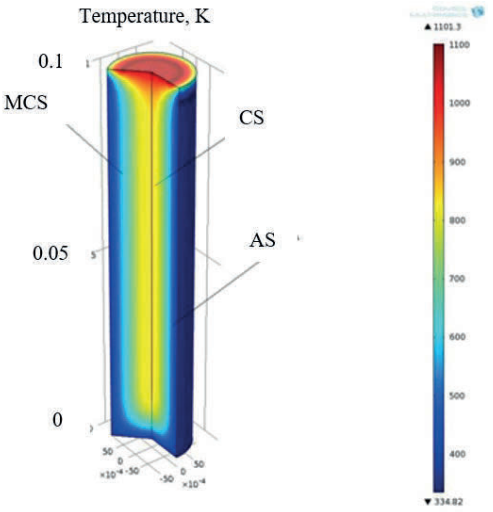

Fig. 8. Temperature field of the $Cu_{45}Ti_{35}Zr_{20}$ melt in the cooling mould: AS – amorphous structure, MCS – microcrystalline structure, CS – crystalline structure.

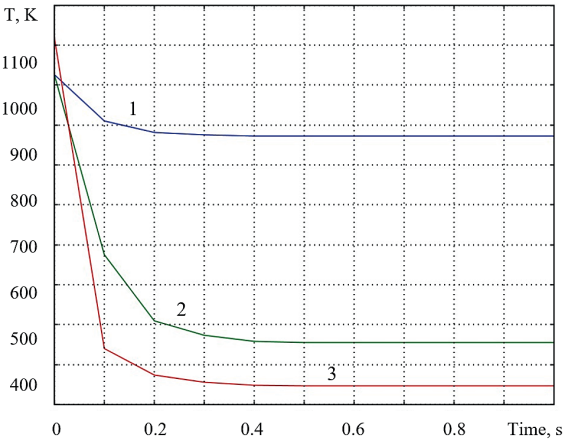

Fig. 9. Temperature distribution in the $Cu_{45}Ti_{35}Zr_{20}$ alloy with a roller surface temperature of 673K: 1 – casting center, 2 – near the cooled mould wall, 3 – near the boundary with the cooling medium.

The presented graphs demonstrate that ultrafast cooling of the metal occurs within 1 second interval. Comparing the data leads to the conclusion that the formation of an amorphous structure across the entire layer is only possible at the maximum cooling rates achieved at the contact boundaries. As the cooling rate decreases, only partial amorphisation occurs, resulting in the formation of both the amorphous (AS) and crystalline (CS) structures near the cooled wall.

Closer to the central part of the casting, due to lower heat dissipation, a MCS structure is formed. Even at the maximum cooling intensity, the formation of an amorphous structure is not observed in the central part of the casting. As the graphs show, for this specific alloy, the amorphous structure can only be obtained near the cooled wall of the mould under maximal heat transfer conditions. The most slowly cooled part of the casting is located on the non-

cooled surface. With an increase in melt thickness, a gradual increase in the crystalline phase (CS) was observed, which is attributed to the increased time the alloy exists in the liquid state. The rate of melt solidification and heat transfer within the metal layer, when convective flows of the liquid melt are present, typically consists of heat transfer by convection and conduction. Thus, the presence of convective flows inside the casting leads to increased heat dissipation and a higher cooling rate, enabling the achievement of a microcrystalline structure with improved mechanical properties.

An additional factor promoting crystallisation is the tendency of zirconium to form ZrO oxides upon reaction with oxygen, which act as crystallisation centres. Molten Zr actively reacts with oxygen to form poorly soluble ZrO oxides. However, when the melt thickness is small, the zirconium does not have enough time to react with oxygen and oxide formation does not occur, as the melt instantaneously transitions to the solid amorphous state. The critical cooling rate R_c of the melt is inversely proportional to the critical thickness of the amorphous alloys. For the $Cu_{45}Ti_{35}Zr_{20}$ alloy, the critical cooling rate was 10^2–10^3 K/s. This rate made it possible to obtain samples with an amorphous structure from the melt, which is confirmed by metallophysical and X-ray structural studies. Amorphous-nanocrystalline structures formed under this rapid quenching possess high mechanical properties, with the alloy hardness reaching 700 HV.

Alloys of the $Ni_{62.4}Nb_{37.6}$ system are highly promising because Nb improves mechanical properties and creep resistance. Niobium is a diffusion-slowing element, which leads to a decrease in the crystal growth rate and contributes to increased structural dispersity. Such alloys exhibit good thermal stability and corrosion resistance [46], [47]. The conditions for solving the thermal casting problem of the $Ni_{62.4}Nb_{37.6}$ alloy and the modelling results (graphs and temperature distribution fields) are presented in Fig. 10.

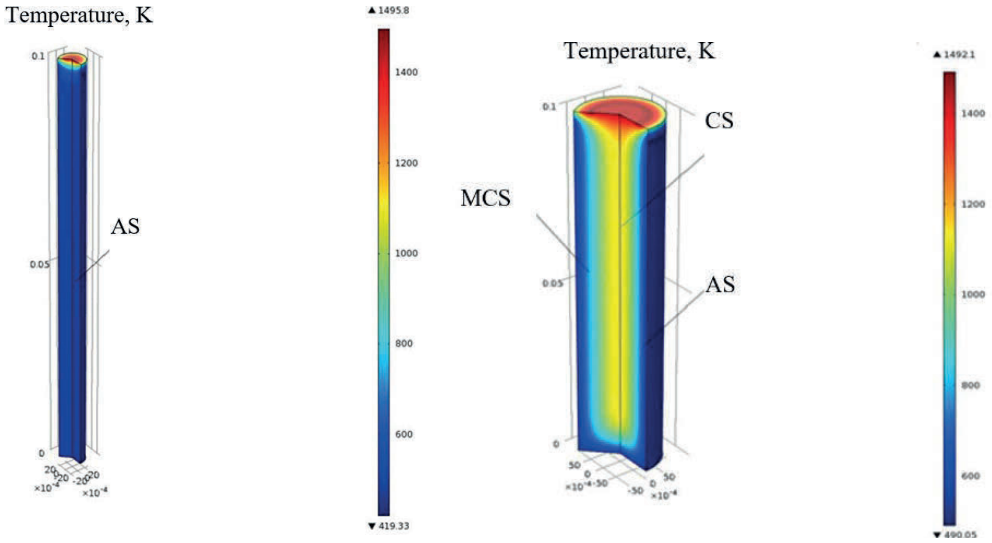

(a) (b)

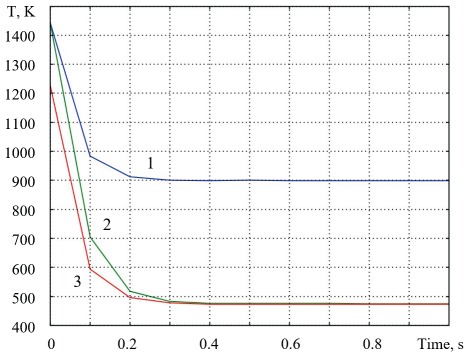

(c)

Fig. 10. Temperature field of the $Ni_{62.4}Nb_{37.6}$: AS – amorphous structure; Dimensions of the liquid ribbon: a) 100mm×3mm, b) 100mm×10mm; c) graph of temperature change over time: 1 – casting centre, 2 – near the cooled mould wall, 3 – near the boundary with the cooling medium.

Modelling results indicate that the formation of the amorphous structure occurs across the entire metal layer (Fig. 10a). This is because the cooling conditions at the mould walls allow for maximal heat dissipation and instantaneous cooling of the melt below the amorphisation temperature of this alloy.

For the $Ni_{62.4}Nb_{37.6}$ alloy, the critical cooling rate was $R_c = 10^2–10^3$ K/s. This rate allowed for the production of alloy samples with an amorphous structure both across the entire cross-section of the casting and partially at the boundaries, which is confirmed by metallophysical studies. The amorphous-crystalline structures formed during this quenching exhibit high mechanical properties, with the alloy hardness reaching 700 HV.

5. CONCLUSION

The modelling and experimental results confirm that amorphous structure formation in the twin-roll casting process is achieved only through the synchronized control of three primary factors: roller gap distance, roller rotation speed, and the temperature of the humid cooling air.

To enhance the degree of amorphisation, an increase in both the cooling air temperature and the roller rotation speed is essential. Crucially, the roller gap distance (critical melt thickness) was identified as the parameter having the maximum influence on the final degree of metal amorphisation, with the highest values achieved at minimal distances. A notable challenge in casting bulk metallic glasses is the spontaneous, localized crystallization observed in certain regions of the casting. The probability of this event is governed by the casting volume and the ratio of the product's thickness to the maximum achievable amorphous thickness δ_{crit} under the given casting conditions. Furthermore, experimental and calculated data confirm that obtaining amorphous products several millimetres thick necessitates alloys possessing a low critical cooling rate R_c, specifically less than 1000 K/s. Metallographic studies revealed that some interior "amorphous" regions are in fact composed of microcrystals, establishing the existence of pseudo-amorphous phases. Overall, it is practically demonstrated that the formation of a true amorphous structure is reliably confined to the layer boundaries under specific melt cooling regimes between the rollers.

REFERENCES

[1] Sharma A., Zadorozhnyy V. Y., Wenrui J., Qiao J. C. Review of thermo-mechanical processing of metallic glasses. *Journal of Non-Crystalline Solids* 2025:666:123714. https://doi.org/10.1016/j.jnoncrysol.2025.123714

[2] Feng Z., Geng H., Zhuang Y., Li P. Progress, Applications, and Challenges of Amorphous Alloys: A Critical Review. *Inorganics* 2024:12(9):232. https://doi.org/10.3390/inorganics12090232

[3] Sohrabi S., Fu J., Li L., Zhang Y., Li X., Sun F., Ma J., Wang W. H. Manufacturing of metallic glass components: Processes, structures and properties. *Progress in Materials Science* 2024:144:101283. https://doi.org/10.1016/j.pmatsci.2024.101283

[4] Stachurski Z. H. On structure and properties of amorphous materials. *Materials* 2011:4:1564–1598.

[5] Zhang G., Hu H., Wu J. Advances in Amorphous Nanomaterials: Synthesis, Characterization and Application. *Materials Today Nano* 2025:32:100675. https://doi.org/10.1016/j.mtnano.2025.100675

[6] Kang J., Yang X., Hu Q., Cai Z., Liu L.-M., Guo L. Recent Progress of Amorphous Nanomaterials. *Chemical Reviews* 2023:123(13):8859–8941. https://doi.org/10.1021/acs.chemrev.3c00229

[7] Han X., Wu G., Du J., Pi J., Yan M., Hong X. Metal and metal oxide amorphous nanomaterials towards electrochemical applications. *Chemical Communications* 2022:58(2):223–237. https://doi.org/10.1039/D1CC04141J

[8] Gao K., Zhu X. G., Chen L., Li W. H., Xu X., Pan B. T., Li W. R., Zhou W. H., Li L., Huang W., Li Y. Recent development in the application of bulk metallic glasses. *Journal of Materials Science & Technology* 2022:131:115–121. https://doi.org/10.1016/j.jmst.2022.05.028

[9] Shao Y., Zhao D., Guo W., Lü S., Wu S. Microstructure optimization of in-situ porous Ti particles reinforced Mg–Cu–Y metallic glass matrix composites via dealloying in metallic melt. *Composites Part B: Engineering* 2025:296:112263. https://doi.org/10.1016/j.compositesb.2025.112263

[10] Zhu S., Schroers J., Curtarolo S., Eckert H., van de Walle A. Special glass structures for first principles studies of bulk metallic glasses. *Acta Materialia* 2024:262:119456. https://doi.org/10.1016/j.actamat.2023.119456

[11] Zhao W., Shan X., Lv W., et al. Quantitative analysis of the microstructure evolution of Al–Fe binary amorphous alloys caused by cooling rates based on atomic bond proportion. *Journal of Materials Science* 2025:60:14160–14170. https://doi.org/10.1007/s10853-025-11236-3

[12] Lebrun N., Dupla F., Bruhier H., Prudent M., Borroto A., Der Loughian C., Bourquard F., Pelletier J-M., Rousseau M., Colombier J.-P., Pierson J.-F., Garrelie F., Steyer P. Metallic glasses for biological applications and opportunities opened by laser surface texturing: A review. *Applied Surface Science* 2024:670:160617. https://doi.org/10.1016/j.apsusc.2024.160617

[13] Halim Q., Mohamed N. A. N., Rejab M. R. M., Naim W. N. W. A., Ma Q. Metallic glass properties, processing method and development perspective: a review. *International Journal of Advanced Manufacturing Technology* 2021:112:1231–1258. https://doi.org/10.1007/s00170-020-06515-z

[14] Wu W., Li X., Liu Q., Hsi Fuh J.Y., Zheng A., Zhou Y., Ren L., Li G. Additive manufacturing of bulk metallic glass: Principles, materials and prospects. *Materials Today Advances* 2022:16:100319. https://doi.org/10.1016/j.mtadv.2022.100319

[15] Yiu P., Diyatmika W., Bönninghoff N., Lu Y. C., Lai B. Z., Chu J. P. Thin film metallic glasses: Properties, applications and future. *Journal of Applied Physics* 2020:127(3). https://doi.org/10.1063/1.5122884

[16] Feng Z., Geng H., Zhuang Y., Li P. Progress, Applications, and Challenges of Amorphous Alloys: A Critical Review. *Inorganics* 2024:12(9):232. https://doi.org/10.3390/inorganics12090232

[17] Jiang R., Da Y., Chen Z., Cui X., Han X., Ke H., Liu Y., Chen Y., Deng Y., Hu W. Progress and perspective of metallic glasses for energy conversion and storage. *Advanced Energy Materials* 2022:12(8):2101092. https://doi.org/10.1002/aenm.202101092

[18] Assouli S., Jabraoui H., Bajjou O., Kotri A., Mazroui M. H., Lachtioui Y. Exploring the impact of cooling rates and pressure on fragility and structural transformations in iron monatomic metallic glasses: Insights from molecular dynamics simulations. *Journal of Non-Crystalline Solids* 2023:621:122623. https://doi.org/10.1016/j.jnoncrysol.2023.122623

[19] Lin X. H., Johnson W. L. Formation of Ti –Zr –Cu – Ni bulk metallic glasses. *Journal of Applied Physics* 1995:78(11):6514–6519.

[20] Ruschel L. M., Gross O., Bochtler B., Li B., Adam B., Neuber N., et al. Ni–Nb–P-based bulk glass-forming alloys: Superior material properties combined in one alloy family. *Acta Materialia* 2023:253:118968.

[21] Shi Y., Feng K., Liu L., He G., Wang B. Numerical Study on the Solidification Microstructure Evolution in Industrial Twin-Roll Casting of Low-Carbon Steel. *Materials* 2025:18(19):4484.

[22] Wang L. X., Zhang C. Y., Liu C. Y., Yan Z., Ran R., Zhang Y. X., Yuan G. Friction Behavior and Wear Mechanism of Twin-Roll Casting $Zr_{55}Cu_{30}Al_{10}Ni_5$ Amorphous Alloy. *Transactions of the Indian Institute of Metals* 2024:77:799–807. https://doi.org/10.1007/s12666-023-02983-5

[23] Zhang C. Y., Yuan G., Zhang Y. X., Wang Y., Fang F., Kang J., Wang G. D. $Zr_{55}Cu_{30}Al_{10}Ni_5$ amorphous alloy sheets with large plasticity fabricated by twin-roll strip casting. *Materials Science and Engineering: A* 2020:794:139904. https://doi.org/10.1016/j.msea.2020.139904

[24] Zhang C. Y., Zhu, Z.W.; Yuan, G.; Wang, Y.Y.; Li, S.T.; Zhang, Y.X.; Li, H.; Li, Z.K.; Zhang, H.F. Solidification behavior and continuous preparation process of high-quality Zr- based metallic glass plates based on twin-roll strip casting. *Journal of Materials Research and Technology* 2024:29:5741–5751. https://doi.org/10.1016/j.jmrt.2024.03.037

[25] Pavlenko A., Koshlak H. Heat and mass transfer during phase transitions in liquid mixtures. *Rocznik Ochrona Srodowiska* 2019:21(1):234–249.

[26] Koshlak H., Pavlenko A. Method of formation of thermophysical properties of porous materials. *Rocznik Ochrona Srodowiska* 2019:21(2):1253–1262.

[27] Pavlenko A. M., Koshlak H. Intensification of gas hydrate formation processes by renewal of interfacial area between phases. *Energies* 2021:14(18):5912.

[28] Pavlenko A., Koshlak H. Production of porous material with projected thermophysical characteristics. *Metallurgical and Mining Industry* 2015:7(1):123–127.

[29] Pavlenko A., Koshlak H., Usenko B. The processes of heat and mass exchange in the vortex devices. *Metallurgical and Mining Industry* 2014:6(3):55–59.

[30] Pavlenko A., Koshlak H., Usenko B. Heat and mass transfer in fluidized layer. *Metallurgical and Mining Industry* 2014:6(6):96–100.

[31] Pavlenko A., Usenko B., Koshlak A. Analysis of thermal peculiarities of alloying with special properties. *Metallurgical and Mining Industry* 2014:6(2):15–19.

[32] Basok B., Davydenko B., Pavlenko A. M. Numerical network modeling of heat and moisture transfer through capillary-porous building materials. *Materials* 2021:14(8):1819.

[33] Assouli S., El Hafi T., El Kharraz A., Bajjou O., Lachtioui Y. Influence of cooling rate and pressure on the structural and mechanical properties of iron monatomic metallic glasses: Insights from molecular dynamics simulations. *Solid State Communications* 2025:399:115883. https://doi.org/10.1016/j.ssc.2025.115883

[34] El Hafi T., Bajjou O., Jabraoui H., Louafi J., Mazroui M., Lachtioui Y. Effects of cooling rate on the glass formation process and the microstructural evolution of Silver mono-component metallic glass. *Chemical Physics* 2023:569:111873. https://doi.org/10.1016/j.chemphys.2023.111873

[35] El Kharraz A., El Hafi T., Assouli S., Samiri A., Kotri A., Bajjou O., Lachtioui Y. Mechanical and structural properties of monatomic zirconium metallic glass under pressure variations and annealing processes: A molecular dynamics study. *Solid State Communications* 2024:392:115644. https://doi.org/10.1016/j.ssc.2024.115644

[36] Pavlenko A., Usenko B., Koshlak A. Thermal conductivity of the gas in small space. *Metallurgical and Mining Industry* 2014:6(2):20–24.

[37] Koshlak H., Pavlenko A. Mathematical model of particle free settling in a vortex apparatus. *Rocznik Ochrona Srodowiska* 2020:22(2):727–734.

[38] Dong Q., Tan J., Li C., Sarac B., Eckert J. Room-temperature plasticity of metallic glass composites: A review. *Composites Part B: Engineering* 2024:280:111453. https://doi.org/10.1016/j.compositesb.2024.111453

[39] Muscas G., Johansson R., George S., Ahlberg M., Arvanitis D., Ahuja R., Scheicher R. H., Jonsson P. E. Unveiling the local structure of the amorphous metal combining first-principles-based simulations and modelling of EXAFS spectra. *Scientific Reports* 2023:13:4983. https://doi.org/10.1038/s41598-023-32051-3

[40] Shen Y., Samwer K., Johnson W. L., Goddard W. A., An Q. Phase formation and phase stability for the homogenous and heterogeneous amorphous metals versus the crystalline phase. Proceedings of the National Academy of Sciences of the United States of America 2025:122(4):e2404489122. https://doi.org/10.1073/pnas.2404489122

[41] Cui C. Y., Liu X. F., Feng L., Xu H. H., Yang J., Cui X. G., Yan H. F. Effects of B content on the microstructure and corrosion resistance of laser cladding $CoCrNiNb_{0.6}B_x$ high-entropy alloy coatings. *Journal of Alloys and Compounds* 2025:1032:181085. https://doi.org/10.1016/j.jallcom.2025.181085

[42] Ming K., Zhu Z., Zhu W., Fang B., Wei B., Liaw P. K., Wei X., Wang J., Zheng S. Enhancing strength and ductility via crystalline-amorphous nanoarchitectures in TiZr-based alloys. *Science Advances* 2022:8(10):eabm2884. https://doi.org/10.1126/sciadv.abm2884

[43] Wang G., Zhang Y., Zou B., Liu Y., Zheng S., Li X., Yan W., Li Z., Wang Y. M. Enhanced plasticity due to melt pool flow induced uniform dispersion of reinforcing particles in additively manufactured metallic composites. *International Journal of Plasticity* 2023:164:103591. https://doi.org/10.1016/j.ijplas.2023.103591

[44] Zhang L., Sun J., Ngan A. H. W., Ning Z., Fan H., Huang Y. Heterogeneity of microstructures in a Cu–Zr based amorphous alloy composite reinforced by crystalline phases. *Composites Part B: Engineering* 2023:262:110823. https://doi.org/10.1016/j.compositesb.2023.110823

[45] Jung H. Y., Yi S. Enhanced glass forming ability and soft magnetic properties through an optimum Nb addition to a Fe–C–Si–B–P bulk metallic glass. *Intermetallics* 2010:18(10):1936–1940.

[46] Koshlak H., Ochrymiuk T. Features of Heat and Mass Transfer in the Thermodynamic Equilibrium Region of Gas Hydrates. *Environmental and Climate Technologies* 2024:28(1):695–711. https://doi.org/10.2478/rtuect-2024-0054

[47] Benedito A. V., Benedetty Torres C. A., Silva R. M. d.C., Krahl P. A., Cardoso D. C. T., Silva F. d. A., Martins C. H. Effects of Niobium Addition on the Mechanical Properties and Corrosion Resistance of Microalloyed Steels: A Review. *Buildings* 2024:14:1462. https://doi.org/10.3390/buildings14051462